Supplementary Material

Direct Growth of two-dimensional phthalocyanine-based COF on Cu-MOF to construct a photoelectrochemical-electrochemical dual-mode biosensing platform for high-efficiency determination of Cr(III)

Shuai Zhang, Kun Chen, Lei Zhu, Miaoran Xu, Yingpan Song, Zhihong Zhang[*],

Miao Du[*]

College of Material and Chemical Engineering, Zhengzhou University of Light

Industry, Zhengzhou 450001, P. R. China

[*]Corresponding authors

E-mail addresses: mainzhh@163.com (Z. Zhang) and dumiao@zzuli.edu.cn (M. Du)

Contents

S1. Experimental section

S1.1 Materials and chemicals

Absolute ethanol, N,N-dimethylformamide (DMF), dimethyl sulfoxide (DMSO), 4-nitro phthalonitrile and chlorobenzene were purchased from Aladdin Chemical Reagent Co. Ltd. (Shanghai, China). $CoCl_2 \cdot 2H_2O$, $Cu(NO_3)_2 \cdot 3H_2O$, sodium sulfide nonahydrate, HCl and NaOH were purchased from Sinopharm Chemical Reagent Co., Ltd. (Shanghai, China). 2,9-Bis[p-(formyl)phenyl]-1,10-phenanthroline and 2,2'-bipyridine-5,5'-dicarboxylicacid were purchased from Shanghai Macklin Biochemical Co., Ltd. All reagents were of analytical grade, and all solutions were prepared with Milli-Q ultrapure water ($\geq$ 18.2 MΩ cm).

S1.2 Pre-treatment of glass carbon electrode (GCE)

Polish the bare glass carbon electrode (GCE, diameter = 3 mm) with alumina powder (0.05 µm), and then wash with piranha solution (H_2O_2 & H_2SO_4: v/v = 3/7), ethanol and water for 10 minutes, and dry under nitrogen at room temperature. After that, GCE was electrochemically activated in 0.5 M H_2SO_4 cycles at -0.2 and 1.6 V potentials, rinsed with water and dried under N_2.

Use 0.05 µm Al_2O_3 slurry to polish the suede to mirror surface, wash off the surface dirt after each polishing, and then move it into an ultrasonic bath for cleaning, each time 2~3 min, repeat three times, and finally use ethanol, HNO_3 and distilled water ultrasonic cleaning. After thorough washing, the electrode should be activated by cyclic voltammetry in a 0.5 M H_2SO_4 solution with a scanning range of 1.0 to -1.0 V, then rinsed with water and dried under N_2.

S1.3 Preparation of all used solutions

0.242 g of KH_2PO_4, 1.45 g of $Na_2HPO_4 \cdot 12H_2O$, 0.200 g of KCl, and 8.003 g of NaCl were dissolved in 1.0 L Milli-Q water to prepare a phosphate buffer solution (PBS, 0.1 M, pH 7.4). Then, 1.600 g of $K_3Fe(CN)_6$, 2.100 g of $K_4Fe(CN)_6$, and 7.500 g of KCl were added into PBS (1.0 L) to obtain an electrolyte solution. The DNA solution (1 mM) was prepared using PBS and diluted to different concentrations of DNA solution (1, 10, 50, 100, and 200 nM). Thereafter, the standard $Cr(NO_3)_3$ solution (1 mM) was diluted using PBS for to form different concentrations of Cr^{3+} solutions (0.1 pM, 1 pM, 10 pM, 0.1 nM, 1 nM, 10 nM, and 100 nM). All solutions were stored in a refrigerator at 4 °C for further use.

S1.4 Synthesis of Cu-MOF

2,2'-Bipyridine-5,5'-dicarboxylic acid (44.0 mg, 0.18 mmol) and $Cu(NO_3)_2 \cdot 3H_2O$ (43.0 mg, 0.18 mmol) were dissolved in a mixed solvent of DMF (3 mL), ethanol (1.5 mL) and chlorobenzene (1.5 mL). Afterward, the mixture was transferred into a Teflon stainless steel autoclave (20 mL) and heated at 126 °C for 60 h. After naturally cooling, the product was washed three times with DMF and absolute ethanol, and dried at 60 °C under vacuum for 8 h.

S1.5 Synthesis of CoPc-PT-COF

CoPc-TA (32 mg, 0.05 mmol) and 2,9-bis[p-(formyl)phenyl]-1,10-phenanthroline (39 mg, 0.1 mmol) were solved in DMSO (10 mL), following by adding acetic acid (50 μL) as catalyst. After ultrasonic treatment for 5 min, the mixture was frozen drying three times and further reacted at 120 °C for 72 h. The final product was washed with

absolute ethanol three times and dried at 70 °C under vacuum for 12 h.

S1.6 Basic characterizations

The surface morphology and nanostructure of the synthesized samples were characterized on JSM-6490LV field emission scanning electron microscope (FE-SEM, Japan) and FEI TECNAI G2 F30 high-resolution transmission electron microscopy (HR-TEM, United States) with a field emission gun of 200 kV. The elemental mapping was measured with energy dispersive X-Ray spectroscopy on high-angle annular dark-field scanning TEM. The specific surface areas of samples were carried out by Brunauer-Emmett-Teller (BET) methods using a Micromeritics ASAP2022 instrument at the temperature of liquid nitrogen. UV-vis spectra were detected on an UV-3900H spectrophotometer (Shimadzu Corporation, Japan) with $BaSO_4$ powder as the reference. Prior to measurement, all samples were degassed at 573 K for 8 h. The chemical components were analyzed by Fourier transform infrared (FT-IR) spectroscopy on a Bruker TENSOR27 spectrometer and X-ray photoelectron spectroscopy (XPS) on an AXIS HIS 165 spectrometer (Kratos Analytical, Manchester, U.K.) with a monochromatized Al Kα X-ray source (1486.71 e KαV photons). Powder X-ray diffraction (PXRD) patterns were taken on a Rigaku D/Max-2500 X-ray diffractometer with Cu Kα radiation ($\lambda = 0.15406$ nm).

S1.7 Electrochemical measurements

Electrochemical impedance spectroscopy (EIS) and cyclic voltammetry (CV) were performed on the Solartron analytical 1470E electrochemical station (U.K.). A conventional three-electrode system is used for measurement including a GCE with a

diameter of 3 mm as the working electrode, an Ag/AgCl (saturated KCl) electrode as a reference electrode, and a platinum slide as a counter electrode. EIS Nyquist plot was obtained in PBS containing 5.0 mM $[Fe(CN)_6]^{3-/4-}$, 0.14 M NaCl, and 0.1 M KCl at a potential of 0.21 V, a frequency range of 100 kHz to 0.1 Hz (**Fig. S1**). **Fig. S1** inset shows the used equivalent circuit including four elements: the solution resistance (R_s), charge-transfer resistance (R_{ct}), constant-phase element (CPE_1), and Warburg impedance (W_1) [1]. CV measurements were executed at a scan rate of 50 mV s^{-1} within the potential range of -0.2 to 0.8 V. All electrochemical measurements are performed at ambient temperature and repeated at least three times. The Zview2 software was used to fit and analyze all EIS Nyquist diagrams, and non-linear least squares were fitted to determine the basic parameters in equivalent circuit.
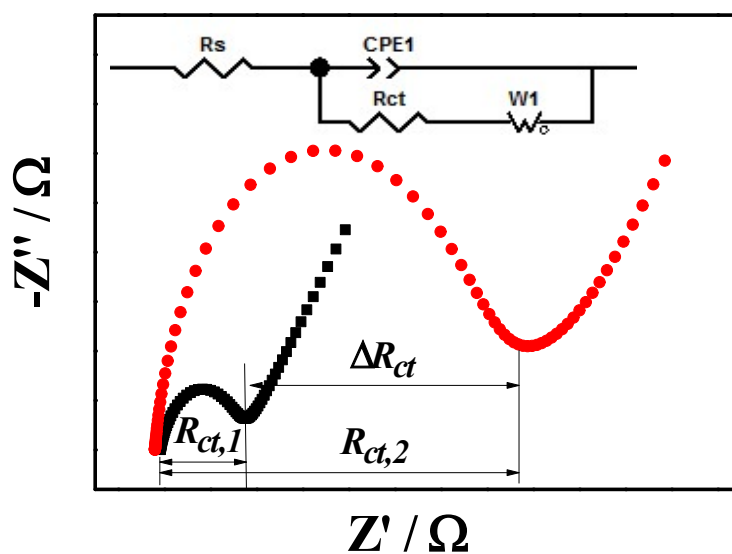
**Fig. S1** Typical EIS Nyquist plots and equivalent circuit.

S2. Basic characterizations of all samples
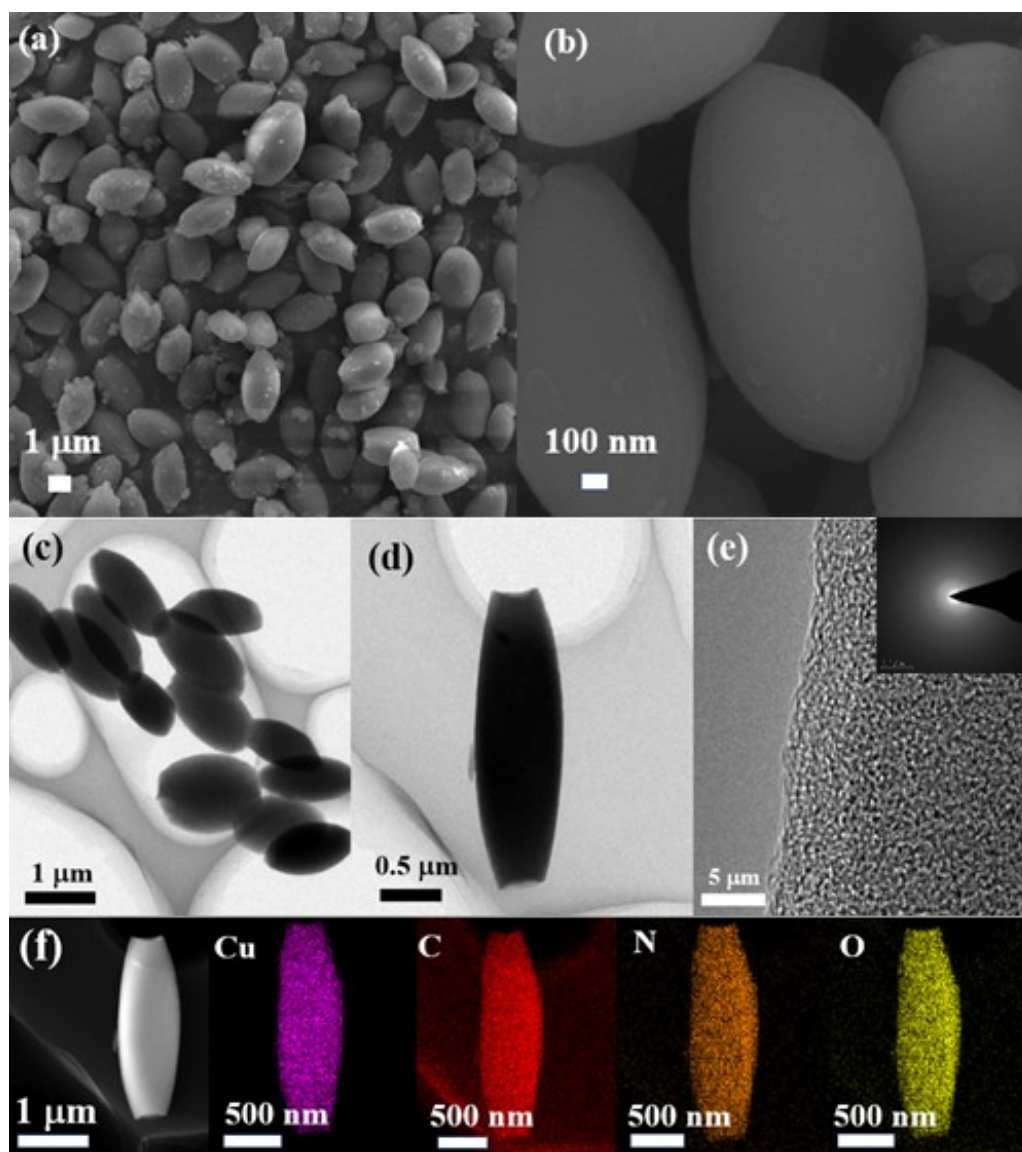
Fig. S2 (a) Low- and (b) high-magnification SEM images, (c, d, e) Low-, high-magnification, and high-resolution TEM images of Cu-MOF (inset: SEAD pattern). (f) EDX mappings of Cu-MOF: Cu (purple), C (red), and N (brown) and O (yellow).

Figs. **S2a** and **b** indicate the SEM images of Cu-MOF, for which the shuttle-like shape of Cu-MOF is found, along with the smooth surface and 2-5 μm in length. This finding is further proven by the TEM image of Cu-MOF (**Fig. S2c**). Apparently, some Cu-MOF ellipsoids do not have ends (**Fig. S2d**), suggesting the incomplete formation of this structure. None clear lattice spacing is observed in the high-resolution TEM (HR-TEM) image of Cu-MOF (**Fig. S2e**), indicating its amorphous nanostructure. It is also confirmed by the SAED pattern (inset of **Fig. S2e**), showing some rings of diffraction planes. Further, the high-angle annular dark field scanning TEM (HAADF STEM) and the EDX mapping show that Cu, C, N, and O elements are uniformly distributed in the Cu-MOF shuttles.
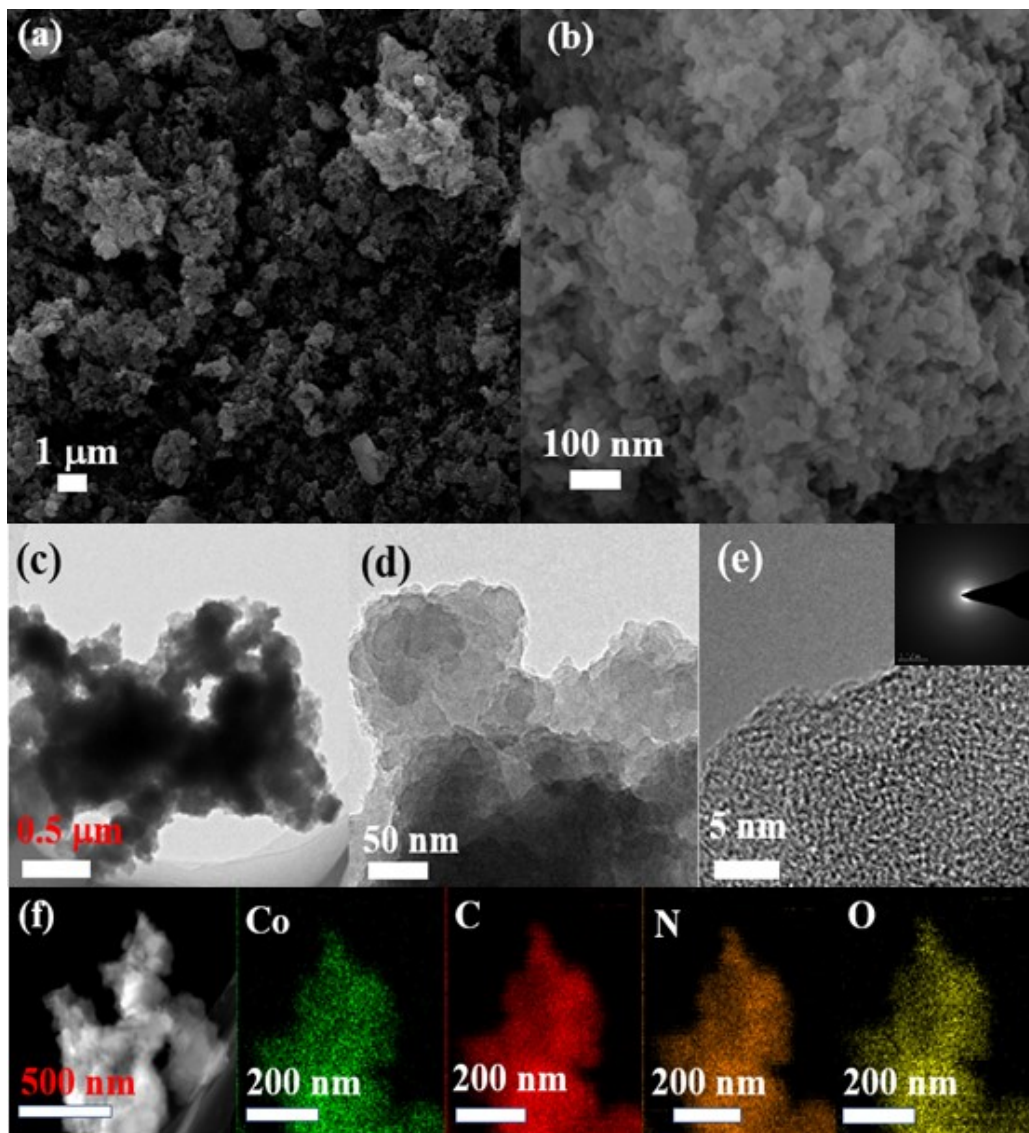
Fig. S3 (a) Low- and (b) high-magnification SEM images, (c, d, e) Low-, high-magnification, and high-resolution TEM images of CoPc-PT-COF. (f) EDX mapping images of CoPc-PT-COF: Co (green), C (red), N (brown) and O (yellow).

Figs. S3a and **b** demonstrate the SEM images of CoPc-PT-COF, which reveals that the CoPc-PT-COF shows the porous nanostructure, comprising irregular nanoparticles. The TEM images of CoPc-PT-COF (**Figs. S3c** and **d**) show the assembled nanoparticles. Meanwhile, no clear lattice spacing is obtained in the HR-TEM of CoPc-

PT-COF (**Fig. S3e**), hinting its low crystallinity, which can be proved by the SEAD pattern (**Fig. S3e** inset). Additionally, the HAADF STEM and EDX elemental mapping images of CoPc-PT-COF reveal that Co, C, N, and O elements are homogenously distributed.
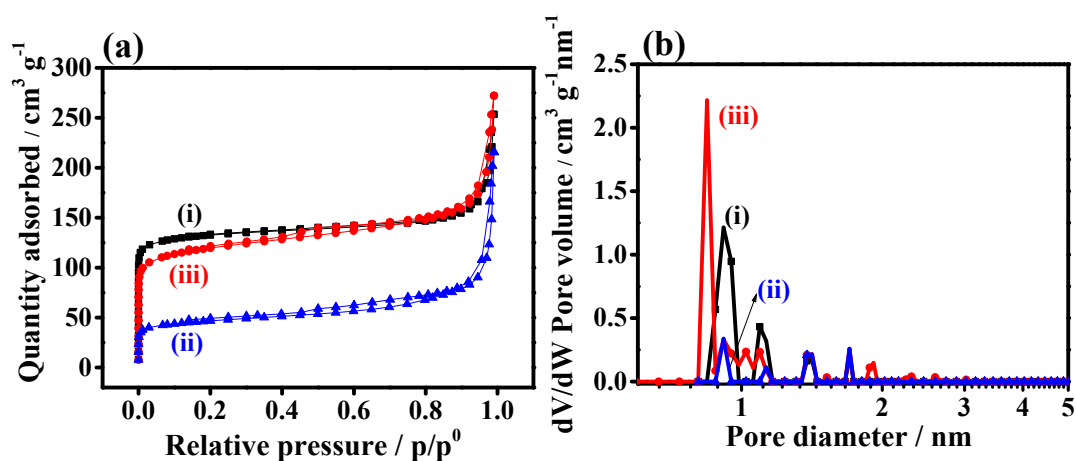

Fig. S4 (a) Nitrogen adsorption-desorption isotherms and (b) NLDFT pore size distribution of Cu-MOF (curve i), CoPc-PT-COF (curve ii), and CoPc-PT-COF@Cu-MOF (curve iii).

Samples	BET surface area ($m^3\ g^{-1}$)	Average pore diameter (nm)
CoPc-PT-COF	159.95	8.34
Cu-MOF	446.03	3.52

| CoPc-PT-COF@Cu-MOF | 407.25 | 4.13 |

Table S1 BET surface areas and pore diameters of CoPc-PT-COF, Cu-MOF, and

CoPc-PT-COF@Cu-MOF.
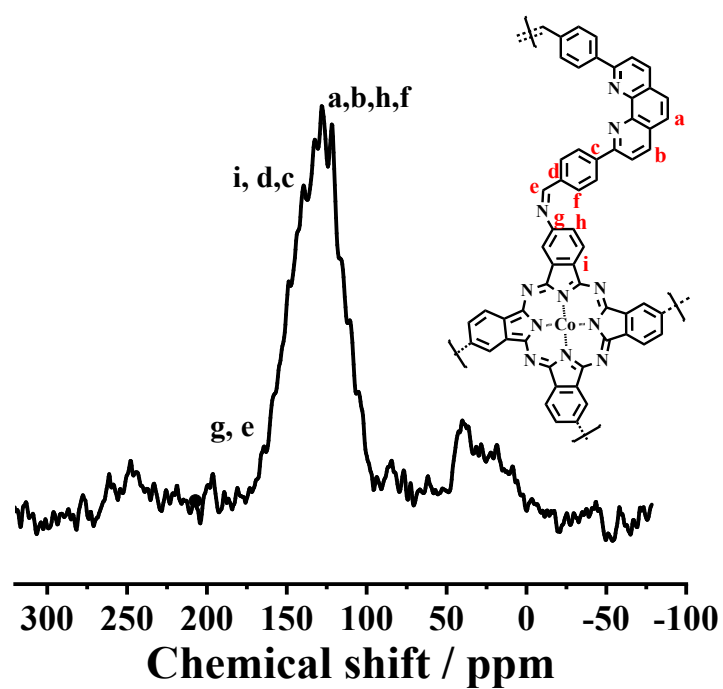


Fig. S5 The Solid-state ^{13}C NMR spectrum of CoPc-PT-COF.
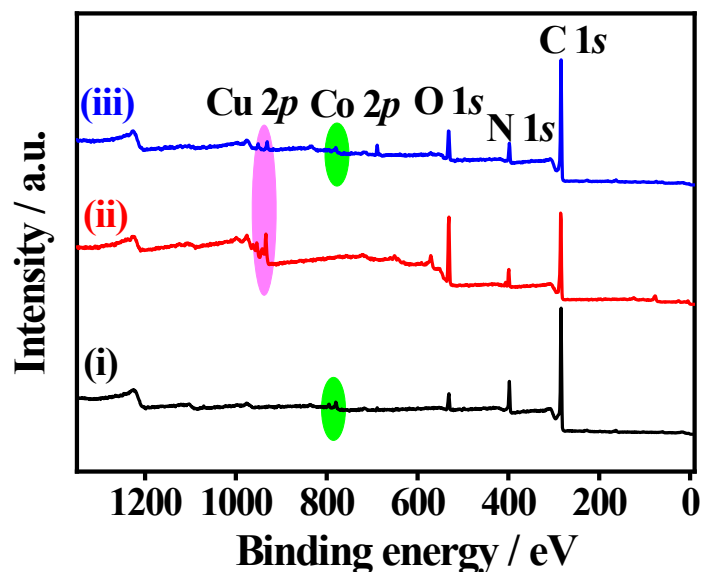
**Fig. S6** XPS survey spectra of CoPc-PT-COF (curve i), Cu-MOF (curve ii), and CoPc-PT-COF@Cu-MOF (curve iii).

The XPS survey scan spectra of the three samples are shown in **Fig. S6**. The clear C $1s$ (284.6 eV), N $1s$ (400 eV), and O $1s$ (530 eV) are presented in the three samples. A weak Cu $2p$ signal (931.5 eV) is observed in Cu-MOF, while the weak Co $2p$ signal (795 eV) is found in CoPc-PT-COF. As expected, both the weak Cu $2p$ and Co $2p$ signals coexist in CoPc-PT-COF@Cu-MOF, indicating the coexistence of two components. The high-resolution XPS spectra of each element in the three samples were studied by Gaussian analysis for probing their chemical environments and detailed components.
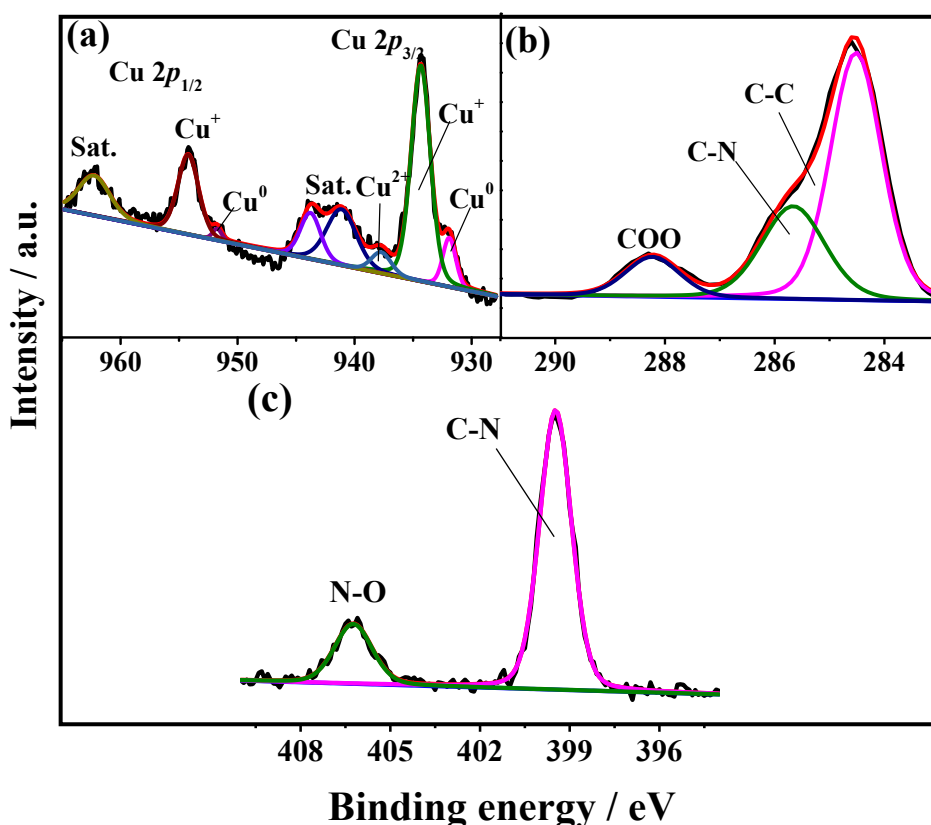
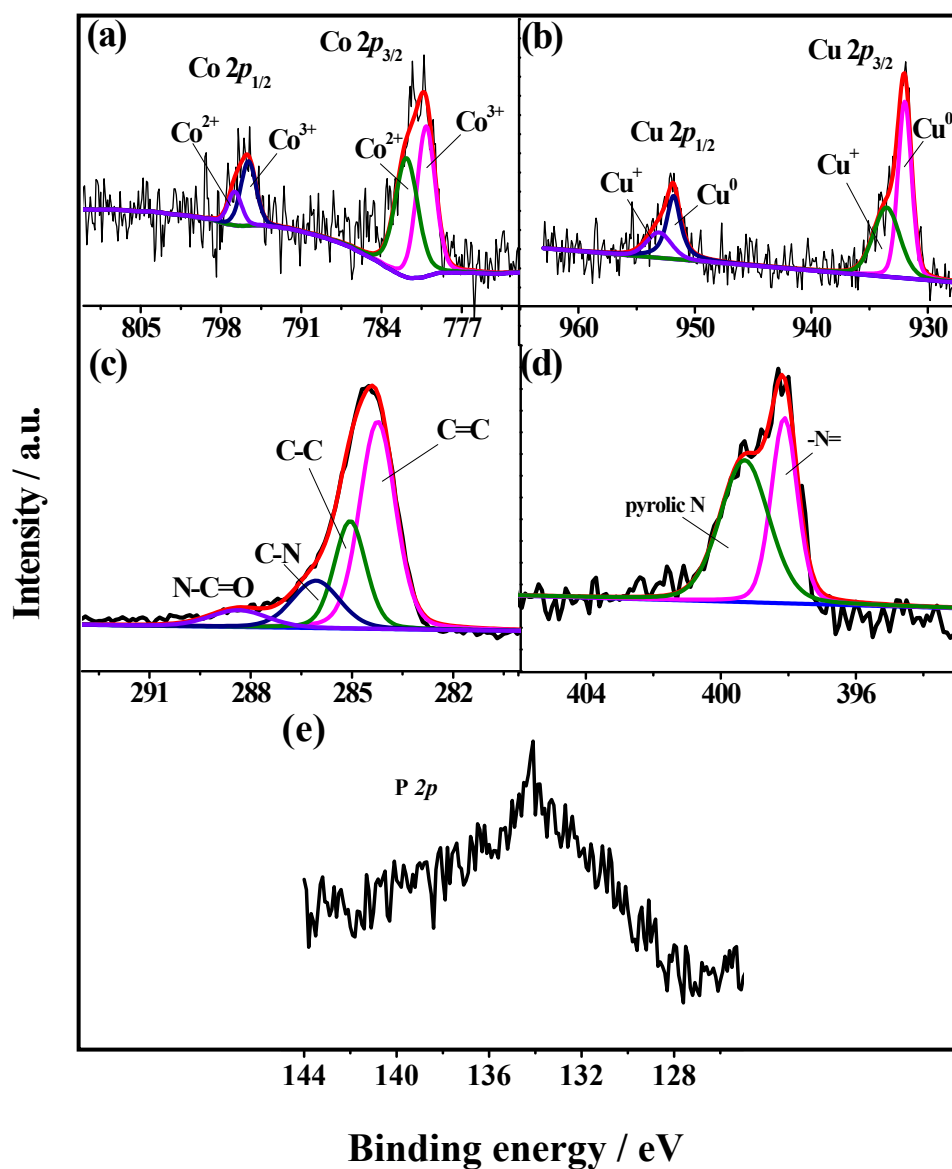**Fig. S7** High-resolution XPS spectra of (a) Cu 2p, (b) C 1s, (d) N 1s, and (d) O 1s in Cu-MOF.

Fig. S7a indicates the Cu XPS spectrum of Cu-MOF, where two couples of peaks at the BE centers of 934.3 and 954.3 eV are obtained for Cu 2$p_{3/2}$ and Cu 2$p_{1/2}$ species, respectively. The Cu 2$p_{3/2}$ component has a main peak at 934.3 eV, due to Cu$^+$, while a higher BE at 937.7 eV (Cu^{2+}) and lower BE at 931.9 eV (Cu^0) are also accompanied. Besides of these, the peaks at the BEs of 941.1 and 943.8 eV are attributed to the shake-up satellite peaks of Cu$^+$ and Cu^{2+} of Cu 2$p_{3/2}$. Meanwhile, apart from the peak of Cu^0 of Cu 2$p_{1/2}$, the main peak of Cu$^+$ at the BE of 954.2 eV and its shake-up satellite peak (962.3 eV) of Cu 2$p_{1/2}$ is observed. Therefore, the mixed valence states of Cu^0/Cu$^+$/Cu^{2+}

coexist in Cu-MOF, which further enhances the electrochemical activity [2]. Three components of C-C, C-N, and COO groups appear in the C 1s XPS spectrum of Cu-MOF (**Fig. S7b**), while two main peaks of C-N and N-O bonds located at 399.5 and 406.3 eV are observed for the N 1s XPS spectrum (**Fig. S7c**).
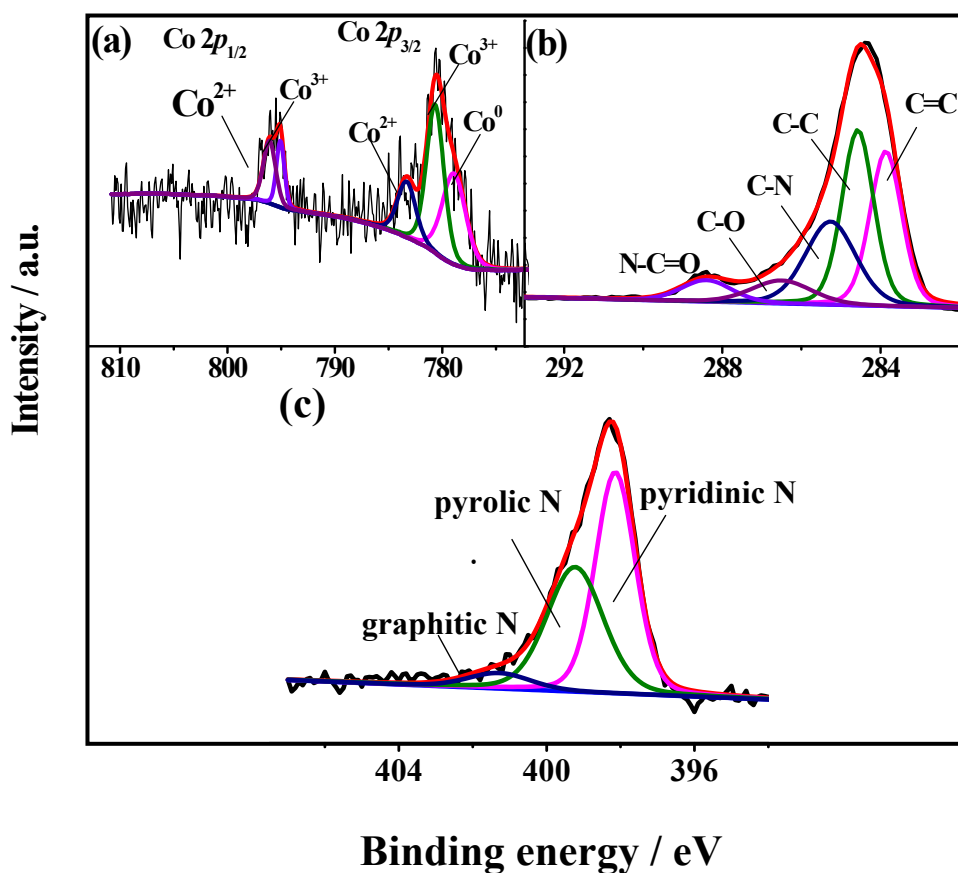
Fig. S8 High-resolution XPS spectra of (a) Co 2*p*, (b) C 1*s*, (d) N 1*s*, and (d) O 1*s* in CoPc-PT-COF.

For CoPc-PT-COF, the same parts of Co 2*p* (**Fig. S8a**) and N 1*s* XPS spectra (**Fig. S8c**) are obtained with those of CoPc-PT-COF@Cu-MOF, while an additional peak at the BE of 286.5 eV is separated in the C 1s XPS spectrum (**Fig. S8b**), corresponding to C-O. Thereby, the chemical structure and component of CoPc-PT-COF is similar with that of CoPc-PT-COF@Cu-MOF owing that only the top layer of CoPc-PT-COF@Cu-MOF can be determined by XPS technique.

Fig. S9 High-resolution XPS spectra of (a) Co 2*p*, (b) Cu 2*p*, (c) C 1*s*, (d) N 1*s*, and (e) P 2*p* in DNA/CoPc-PT-COF@Cu-MOF.

In prior to the study of DNA strands sorption on CoPc-PT-COF@Cu-MOF hybrid, the variation in the chemical structures and components of the hybrid before and after the DNA immobilization was probed by XPS characterization. As depicted in **Fig. S9**, no apparent change in Co 2*p* XPS deconvolution is found (**Fig. S9a**), while Cu^{2+} species

at the BEs of 933.5 and 953.1 eV are obverted in the Cu $2p$ XPS (**Fig. S9b**), due to Cu^{2+} $2p_{3/2}$ and Cu^{2+} $2p_{1/2}$, respectively. This hints that partial Cu^0 species are oxidized during the DNA immobilization. Also, no substantial change in C $1s$ XPS spectrum is achieved, but without the observation of $\pi-\pi^*$ bond (**Fig. S9c**). The absence of –N= group is also obtained in N $1s$ XPS spectrum (**Fig. S9d**). These results reveal the coverage of DNA strands on the hybrid network. Particularly, the appearance of the P $2p$ XPS signal (**Fig. S9e**) also proves the successful immobilization of DNA.
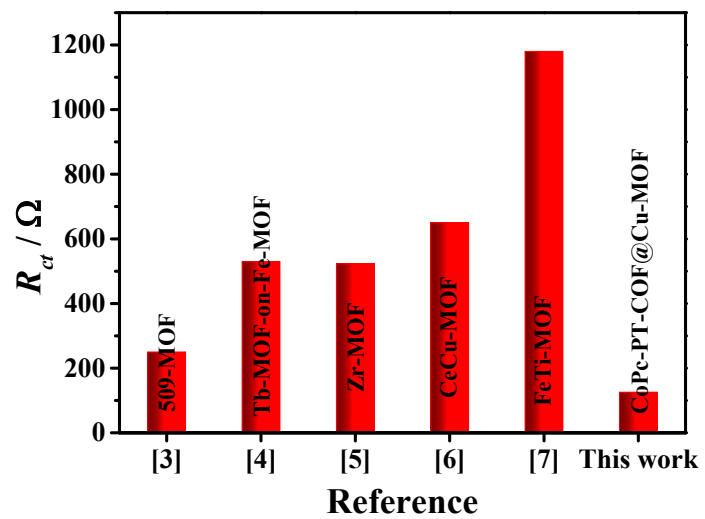
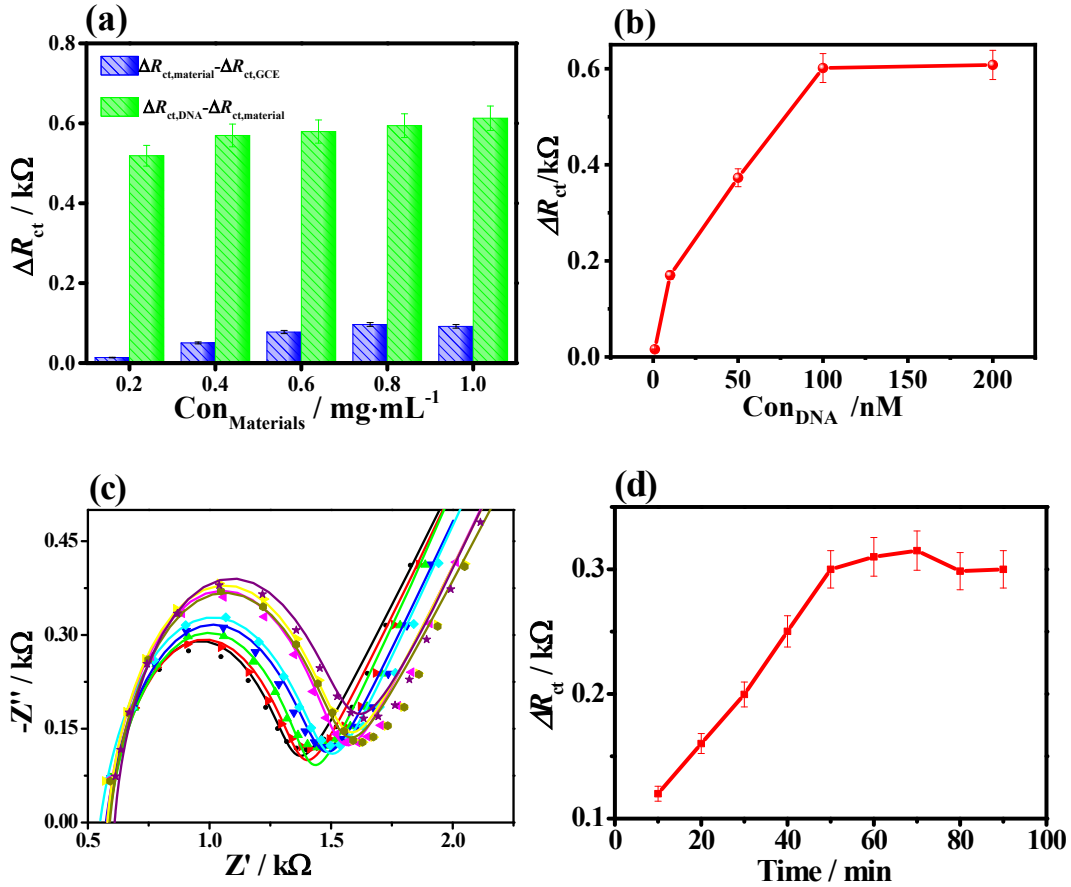**Fig. S10** Comparison the electrochemical activity of CoPc-PT-COF@Cu-MOF with other MOFs and COFs [3-7].

S3. Sensing performances of the prepared biosensors
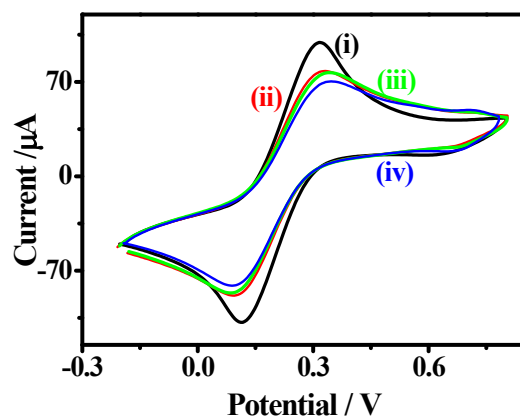
Fig. S11 CV curves during the construction of CoPc-PT-COF@Cu-MOF-based biosensor for detecting Cr^{3+} ions (10 pM): (i) GCE, (ii) CoPc-PT-COF@Cu-MOF/GCE, (iii) DNA/CoPc-PT-COF@Cu-MOF/GCE, and (iv) Cr^{3+}/DNA/CoPc-PT-COF@Cu-MOF/GCE.

Fig. S12 (a) Effect of CoPc-PT-COF@Cu-MOF dosage on biosensor fabrication and Cr^{3+} detection, as revealed by ΔR_{ct} values for each step. (b) Effect of DNA concentration on Cr^{3+} detection, as illustrated by ΔR_{ct} values for Cr^{3+} detection. (c) EIS Nyquist plots of the CoPc-PT-COF@Cu-MOF-based biosensor for detection of Cr^{3+}, recorded at different binding times of Cr^{3+} and (d) the corresponding ΔR_{ct} values obtained at different binding times.

**Fig. S12a** shows the EIS responses of different biosensors constructed by coating the CoPc-PT-COF@Cu-MOF suspension at different concentrations (0.2, 0.4, 0.6, 0.8, and 1 mg mL^{-1}) for detection of Cr^{3+}. The EIS responses (ΔR_{ct}) increase with increasing the dosage of CoPc-PT-COF@Cu-MOF. This finding suggests more DNA strands can be anchored over the thicker CoPc-PT-COF@Cu-MOF layer, thus leading to more

sensitive detection of Cr^{3+}. When the dosage of CoPc-PT-COF@Cu-MOF is larger than

1 mg mL^{-1}, the EIS response for detection of Cr^{3+} is up to equilibrium. That is, too thick

CoPc-PT-COF@Cu-MOF layer is apt to fall from the electrode due to the poor coating

interaction. Therefore, the optimal usage of CoPc-PT-COF@Cu-MOF was set as 1 mg

mL^{-1}, which was used in the further electrochemical measurements.

In addition, the CoPc-PT-COF@Cu-MOF-based biosensors developed by

anchoring DNA strands with diverse concentrations were applied for detecting Cr^{3+}.

Fig. S12b illustrates that the ΔR_{ct} values increase with increasing the DNA

concentration. When the DNA concentration is larger than 100 nM, the ΔR_{ct} value

obtained from the detection of Cr^{3+} levels off. It hints at the interaction between DNA

strands and Cr^{3+} achieves a platform. When the modified electrode was incubated with

DNA of a large concentration, much more DNA strands can be immobilized due to the

complex effect. Owing to the presence of the negative phosphate groups bearing on the

anchored DNA strands, the repulsion interaction between DNA strands hampers their

further adsorption [8, 9]. Thus, the optimal DNA concentration was as 100 nM, which was

also explored for the further construction of biosensors for analyzing Cr^{3+}.

The incubation time of the construction of biosensor in Cr^{3+} solution also plays an

essential role. **Fig. S12c** shows the series of ΔR_{ct} values calculated from the detection

of Cr^{3+} ions using the developed biosensor are recorded at the diverse incubation time.

The ΔR_{ct} value substantially increases at the beginning. After the binding time is longer

than 1 h, the ΔR_{ct} value is up to equilibrium, hinting that the coordination interaction

between Cr^{3+} and DNA strands is saturated. Hence, the optimal binding time of Cr^{3+}

and DNA strands is 1 h for ensuring their complete binding.
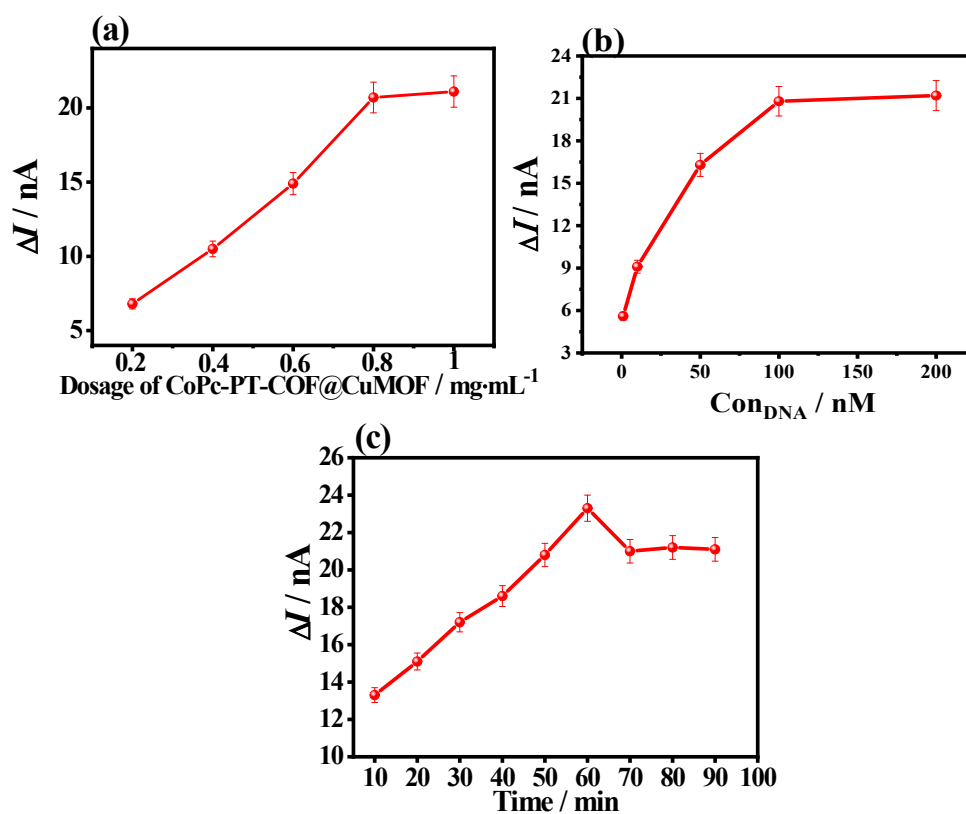
Fig. S13 The effect of (a) CoPc-PT-COF@Cu-MOF concentrations, (b) DNA

concentrations and (c) incubation time of Cr^{3+} based PEC biosensor.

S4. Real sample analysis

Spiked amount (pM)	Found amount (pM)	Apparent Recovery (%)	RSD (%)
0.10	0.09	98.90	1.27
1.00	1.01	101.10	1.54
10.00	9.89	98.90	1.43
100.00	112.81	112.81	1.24
1000.00	1031.24	103.12	1.15
10000.00	9363.29	93.63	1.03
100000.00	102223.00	102.22	1.86

Table S2 The concentration of Cr^{3+} in river water detected by the EC biosensor ($n = 3$).

Table S3 The concentration of Cr^{3+} in tap water detected by the EC biosensor ($n = 3$).

Spiked amount (pM)	Found amount (pM)	Apparent Recovery (%)	RSD (%)
0.10	0.10	100.00	1.69
1.00	1.00	100.40	1.28
10.00	10.09	100.90	1.06
100.00	98.69	98.69	1.18
1000.00	995.62	99.62	1.06
10000.00	10448.35	104.48	2.05
100000.00	114062.50	114.06	2.05

Table S4 The concentration of Cr^{3+} in river water detected by the PEC biosensor ($n = 3$).

Spiked amount (pM)	Found amount (pM)	Apparent Recovery (%)	RSD (%)
0.10	0.09	90.00	0.50
1.00	0.90	90.00	0.30
10.00	10.96	109.60	0.20
100.00	91.20	91.20	0.20
1000.00	1047.13	104.71	0.60
10000.00	10092.53	100.93	0.30
100000.00	95499.26	95.50	0.70

Table S5 The concentration of Cr^{3+} in tap water detected by the PEC biosensor ($n = 3$).

Spiked amount (pM)	Found amount (pM)	Apparent Recovery (%)	RSD (%)
0.10	0.09	90.00	0.50
1.00	1.05	104.70	0.20
10.00	10.94	109.40	0.20
100.00	95.50	95.50	0.30
1000.00	1020.94	102.09	0.60
10000.00	10471.28	104.71	0.30
100000.00	91201.08	91.20	0.60

References

1.   Z. Lukács and T. Kristóf, *Electrochim. Acta*, 2020, **363**, 137199.

2.   L. Majidi, A. Ahmadiparidari, N. Shan, S. N. Misal, K. Kumar, Z. Huang, S. Rastegar, Z. Hemmat, X. Zou, P. Zapol, J. Cabana, L. A. Curtiss and A. Salehi-Khojin, *Adv. Mater.*, 2021, **33**, 2004393.

3.   Z.-H. Zhang, F.-H. Duan, J.-Y. Tian, J.-Y. He, L.-Y. Yang, H. Zhao, S. Zhang, C.-S. Liu, L.-H. He, M. Chen, D.-M. Chen and M. Du, *ACS Sensors*, 2017, **2**, 982-989.

4.   F. Su, S. Zhang, H. Ji, H. Zhao, J.-Y. Tian, C.-S. Liu, Z. Zhang, S. Fang, X. Zhu and M. Du, *ACS Sensors*, 2017, **2**, 998-1005.

5.   S. Wang, Z. Li, F. Duan, B. Hu, L. He, M. Wang, N. Zhou, Q. Jia and Z. Zhang, *Anal. Chim. Acta*, 2019, **1047**, 150-162.

6.   M. Wang, Y. Liu, L. Yang, K. Tian, L. He, Z. Zhang, Q. Jia, Y. Song and S. Fang, *Sensor. Actuat. B-Chem.*, 2019, **281**, 1063-1072.

7.   M. Wang, M. Hu, Z. Li, L. He, Y. Song, Q. Jia, Z. Zhang and M. Du, *Biosens. Bioelectron.*, 2019, **142**, 111536.

8.   M. Lv, W. Zhou, H. Tavakoli, C. Bautista, J. Xia, Z. Wang and X. Li, *Biosens. Bioelectron.*, 2021, **176**, 112947.

9.   X. Liu, Y. Zhao and F. Li, *Biosens. Bioelectron.*, 2021, **173**, 112832.